Thin film flow over flexible membranes containing surface texturing: bio-inspired solutions

Y.C. Lee, H.M. Thompson, P.H. Gaskell[1]

School of Mechanical Engineering, The University of Leeds, Leeds, LS2 9JT, United Kingdom.

Abstract

Gravity-driven continuous thin liquid film flow over a flexible membrane containing surface topography is modelled using lubrication theory. The associated coupled nonlinear equation set, for the film thickness, pressure and membrane deflection, is solved using a state-of-the-art full approximation storage (FAS) multigrid algorithm with automatic mesh refinement and adaptive time-stepping, in order to maximise computational efficiency when fine-scale resolution is required while ensuring accurate mesh independent solutions at the micro-scale. The robustness of the approach is demonstrated through the solution of a series of problems and comparisons drawn with the same flow on an equivalent completely rigid membrane. It is shown that the former differs considerably from the latter in that the film thickness affects the shape of the flexible membrane, the compliance of which in turn impinges on the profile of the resulting free-surface disturbance.

Key words: Thin film flow, Flexible membrane, Lubrication theory, Adaptive mesh refinement, Adaptive time-stepping, Multigrid

1. Introduction

The past few years have seen several examples of mankind turning to nature for bio-inspired solutions to challenging practical problems across a

Email addresses: y.c.lee@leeds.ac.uk, h.m.thompson@leeds.ac.uk, p.h.gaskell@leeds.ac.uk (Y.C. Lee, H.M. Thompson, P.H. Gaskell[1])

[1]Corresponding author

broad swathe of engineering and science [1]; natural and manufactured surfaces containing complex micro-scale patterning/texture having emerged as a prominent area of research [2] [3]. In an engineering context, thin film flow over surface patterning is present in a variety of processes involving printing/photo-lithography [4] and the application of precision protective coatings [5]; while in biological systems they occur in such diverse areas as plant disease control [6], redistribution of lung linings in respiratory systems [7] and in sustaining life itself as in the case of the Namibian fog-basking beetle which drinks by harvesting morning mists that condense on the upper surface of its exoskeleton [8].

To date, such three-dimensional micro-scale fluid flow problems have proved extremely problematic to explore experimentally [9], hence the current dearth of important data for providing the insight necessary to improve existing man-made functional surfaces and to point the way forward in the development of new ones that mimic nature itself. Similarly, the modelling of them is at an early stage of development, with lubrication theory currently providing the vital underpinning; only a particular class of problems has been computed accurately for the case of idealised rigid surfaces containing well defined and sparsely distributed topographical features [10] [11] [12] .

Despite the above achievements, the equally relevant and arguably more important case of flow on patterned/textured flexible membranes has received very little attention. Examples of these include replication of the surfaces of natural leaves for enhanced micro-scale tribological properties [13] the self-assembly of biomimetic antireflection coatings [14] and the fabrication of silicon optoelectric devices on curved surfaces - that is, electronic eyeballs [15]. This is not surprising since thin film flow on flexible membranes presents a further complication to those associated with rigid substrates, since it gives rise to a coupled solid-fluid interaction, which any model of such a system must embody.

The thrust of this paper, therefore, is the formulation of a model for predicting thin film flow over flexible membranes containing well defined topographical features and the efficient, accurate solution of the same using state-of-the-art numerical methods. The problem is formulated in Section 2, followed by an outline of the method of solution in Section 3. Results are presented in Section 4 where comparisons are drawn with solutions for the case of a rigid membrane, clearly demonstrating the influence of the fluid film thickness on the shape of the flexible membrane and the compliance of the latter on the profile of the corresponding free-surface disturbance.

Conclusions are drawn in Section 5.

2. Problem Specification

The problem of interest is formulated in terms of the long-wavelength lubrication approximation, resulting in a set of three coupled equations for the film thickness, pressure and membrane deflection. For the sake of simplicity the liquid is assumed Newtonian and incompressible, with constant density, ρ_f, viscosity, μ, and surface tension, σ; while the flexible membrane is taken to be homogeneous, infinitely long and thin (thickness, Λ) with uniform tension, ζ, in the longitudinal and transverse directions, and to have constant density, ρ_m, and damping coefficient, η.

Figure 1 is a schematic of the motion of such a thin liquid film, of thickness $H(X,Y,T)$, over a flexible membrane, given by $S(X,Y,T) = D(X,Y,T) + E(X,Y,T)$, inclined at an angle θ to the horizontal and containing, for illustration purposes, a single trench topography, $D_0 \ll H_0$, where H_0 is the undisturbed fully-developed asymptotic film thickness for a constant volumetric flow, $Q_0 = H_0^3 \rho_f g \sin\theta/(3\mu)$ per unit width; $D(X,Y,T)$ characterises the height/depth of the topography present while $E(X,Y,T)$ represents the deflection of the membrane.

Neglecting inertia effects, the flow is governed by the Stokes and continuity equations, viz

$$\rho_f \frac{\partial \underline{U}}{\partial T} = -\nabla P + \mu \nabla^2 \underline{U} + \rho_f \underline{g} \ , \tag{1}$$

$$\nabla . \underline{U} = 0 \ , \tag{2}$$

where $\underline{U} = (U,V,W)$ and P are the fluid velocity and pressure respectively, T is the time and $\underline{g} = g(\sin\theta, 0, -\cos\theta)$ is the acceleration due to gravity, together with

$$\rho_m \Lambda \left(\frac{\partial^2 E}{\partial T^2} + \eta \frac{\partial E}{\partial T} \right) - \zeta \nabla^2 E = -(\rho_m \Lambda g + \rho_f \Psi g)\cos\theta + \sigma \nabla^2 \Psi \ , \tag{3}$$

for the deflection of the membrane, where $\Psi(X,Y,T) = H + S$ is the sum of the liquid film and membrane heights. The latter equation relates the deflection of the membrane to the corresponding hydrostatic and capillary pressure terms. The boundary conditions which close the problem consist of no-slip at the surface of the membrane, $Z = S$, together with the usual stress and kinematic conditions at the free surface, $Z = \Psi$.

By introducing the following non-dimensional variables

$$(h, s, \psi, \lambda, d, e) = \frac{(H, S, \Psi, \Lambda, D, E)}{H_0}, \quad (x, y) = \frac{(X, Y)}{L_0}, \quad z = \frac{Z}{H_0},$$
$$p(x, y, t) = \frac{2P}{\rho_f g L_0 \sin\theta}, \quad (u, v, w) = (\frac{U}{U_0}, \frac{V}{U_0}, \frac{W}{\epsilon U_0}), \quad t = \frac{U_0 T}{L_0},$$

with $\varepsilon = H_0/L_0 \ll 1$, and imposing the specified boundary conditions, equations (1)–(3) reduce to the following coupled set

$$\frac{\partial \psi}{\partial t} = \frac{\partial}{\partial x}\left[\frac{h^3}{3}\left(\frac{\partial p}{\partial x} - 2\right)\right] + \frac{\partial}{\partial y}\left[\frac{h^3}{3}\left(\frac{\partial p}{\partial y}\right)\right] , \quad (4)$$

$$p = -\frac{6}{\beta^3}\nabla^2(h+s) + \frac{2}{\beta}6^{1/3}N(h+s) , \quad (5)$$

$$-\Upsilon\left(\frac{\partial^2 e}{\partial x^2} + \frac{\partial^2 e}{\partial y^2}\right) = -\left(\psi + \frac{\rho_m}{\rho_f}\lambda\right)\mathrm{Bo}\cos\theta + \frac{\partial^2 \psi}{\partial x^2} + \frac{\partial^2 \psi}{\partial y^2} , \quad (6)$$

when terms of $O(\varepsilon^2)$ and higher are neglected. $N = \mathrm{Ca}^{1/3}\cot\theta$, where $\mathrm{Ca} = \mu U_0/\sigma$ is the Capillary number defined in terms of the free-surface velocity $U_0 = 3Q_0/(2H_0)$, and indicates the relative importance of the normal component of gravity [16]; $\mathrm{Bo} = \rho_f g L_0^2/\sigma$ is the Bond number, a measure of the ratio of gravitational to surface tension forces; $\Upsilon = \zeta/\sigma$ is the ratio of membrane tension to surface tension.

In deriving the above, the ambient pressure datum is assumed to be zero and implicit in the choice of scaling is the assumption $\theta \neq 0$, that is the membrane is never horizontal. L_0 is the characteristic in-plane length scale which is proportional to the capillary length, L_c, given by

$$L_0 = \beta\left(\frac{\sigma H_0}{3\rho_f g \sin\theta}\right)^{1/3} = \frac{H_0}{(6\mathrm{Ca})^{\frac{1}{3}}} \quad \text{and} \quad \beta = L_0/L_c , \quad (7)$$

The required accompanying boundary conditions of no-slip at the surface of the membrane and zero tangential stresses at the free-surface are

$$(u, v) = (0, 0) \text{ at } z = s \quad \text{and} \quad \frac{\partial u}{\partial z} = \frac{\partial v}{\partial z} = 0 \text{ at } z = \psi , \quad (8)$$

together with fully developed flow conditions far upstream

$$\psi(x = 0, y) = 1 . \quad (9)$$

In addition, zero flux is imposed at the stream- and span-wise boundaries such that gradients in h and p and dirichlet conditions for e there are zero.

Topography depth/height, d, is defined via arc-tangent functions which enable the side steepness to be controlled easily, thus allowing the creation of simple primitive shapes [12]. For example, the rectangular trench topography, shown in Figure 1, of length l_t, width w_t and height d_0 centred at (x_t, y_t), is specified by defining

$$\begin{aligned} d(x,y) &= \frac{d_0}{b_0}\left[\tan^{-1}\left(\frac{-a_x - l_t/2}{\gamma l_t}\right) + \tan^{-1}\left(\frac{a_x - l_t/2}{\gamma l_t}\right)\right] \times \\ &\quad \left[\tan^{-1}\left(\frac{-a_y - w_t/2}{\gamma w_t}\right) + \tan^{-1}\left(\frac{a_y - w_t/2}{\gamma w_t}\right)\right] , \end{aligned} \tag{10}$$

where γ is the adjustable parameter used to control topography steepness, while $A = w_t/l_t$ is the aspect ratio with

$$b_0 = 4\tan^{-1}\left(\frac{1}{2\gamma}\right)\tan^{-1}\left(\frac{A}{2\gamma}\right) ; \tag{11}$$

the local topography co-ordinates in the x and y directions are given by

$$a_x = x_t - x , \quad \text{and} \quad a_y = y_t - y . \tag{12}$$

Equation (10) can be used to specify most simple primitive topographies by modifying a_x and a_y appropriately. It is then relatively straightforward to add/subtract primitives to create complex interconnected topographical patterns.

3. Method of Solution

The numerical method employed to solve equations (4)–(6) subject to the the attendant boundary conditions is described in detail in [12]; accordingly only a brief overview of the important features is provided here.

3.1. Spatial and Temporal Discretisation

Equations (4)–(6), written in terms of the following finite difference expressions, were solved at each node (i, j) of the rectangular domain, $(x, y) \in$

Ω, with the same uniform grid spacing, Δ, in the x and y directions

$$\begin{aligned}
\frac{\partial \psi_{i,j}}{\partial t} &= \frac{1}{\Delta^2}\left[\left.\frac{h^3}{3}\right|_{i+\frac{1}{2},j}(p_{i+1,j}-p_{i,j}) - \left.\frac{h^3}{3}\right|_{i-\frac{1}{2},j}(p_{i,j}-p_{i-1,j}) + \right. \\
&\left. \left.\frac{h^3}{3}\right|_{i,j+\frac{1}{2}}(p_{i,j+1}-p_{i,j}) - \left.\frac{h^3}{3}\right|_{i,j-\frac{1}{2}}(p_{i,j}-p_{i,j-1})\right] - \\
&\frac{2}{\Delta}\left(\left.\frac{h^3}{3}\right|_{i+\frac{1}{2},j} - \left.\frac{h^3}{3}\right|_{i-\frac{1}{2},j}\right), \qquad (13) \\
p_{i,j} &= -\frac{6}{\beta^3\Delta^2}\left[(h_{i+1,j}+s_{i+1,j}) + (h_{i-1,j}+s_{i-1,j}) + (h_{i,j+1}+s_{i,j+1}) + \right. \\
&\left. (h_{i,j-1}+s_{i,j-1}) - 4(h_{i,j}+s_{i,j})\right] + \frac{2\sqrt[3]{6}N}{\beta}(h_{i,j}+s_{i,j}) \ , \qquad (14) \\
e_{i,j} &= \frac{1}{4}\left(e_{i+1,j}+e_{i-1,j}+e_{i,j+1}+e_{i,j-1}\right) - \frac{\Delta^2}{4\Upsilon}\left[\left(\psi_{i,j}+\frac{\rho_m}{\rho_f}\lambda_{i,j}\right)Bo\cos\theta \right. \\
&\left. - \left(\frac{\psi_{i+1,j}+\psi_{i-1,j}+\psi_{i,j+1}+\psi_{i,j-1}-4\psi_{i,j}}{\Delta^2}\right)\right] , \qquad (15)
\end{aligned}$$

together with

$$\begin{aligned}
h_{i,j} &= \psi_{i,j} - s_{i,j} \ , \qquad (16) \\
s_{i,j} &= d_{i,j} + e_{i,j} \ . \qquad (17)
\end{aligned}$$

The terms, $\frac{h^3}{3}|_{i\pm\frac{1}{2},j}$, $\frac{h^3}{3}|_{i,j\pm\frac{1}{2}}$ are pre-factors obtained from linear interpolation between neighbouring nodes.

Time integration was carried out using the standard, second-order accurate Crank-Nicholson method. Re-writing the right hand side of equation (13) as $F(h_{i,j}, p_{i,j}, h_{i\pm1,j}, p_{i\pm1,j}, h_{i,j\pm1}, p_{i,j\pm1})$ leads to an equation of the form

$$\begin{aligned}
&\psi_{i,j}^{n+1} - \frac{\Delta t^{n+1}}{2}F(h_{i,j}^{n+1}, p_{i,j}^{n+1}, h_{i\pm1,j}^{n+1}, p_{i\pm1,j}^{n+1}, h_{i,j\pm1}^{n+1}, p_{i,j\pm1}^{n+1}) \\
&= \psi_{i,j}^{n} + \frac{\Delta t^{n+1}}{2}F(h_{i,j}^{n}, p_{i,j}^{n}, h_{i\pm1,j}^{n}, p_{i\pm1,j}^{n}, h_{i,j\pm1}^{n}, p_{i,j\pm1}^{n}), \qquad (18)
\end{aligned}$$

for which $\Delta t^{n+1} = t^{n+1} - t^n$; the right hand side is given in terms of known values at the end of the nth time step, $t = t^n$.

3.2. Multigrid strategy

Equations (13)–(17) were solved accurately and efficiently using a full approximation storage (FAS) algorithm. Following the multigrid approach employed in [12], a sequence of progressively finer grids ($\mathcal{G}_k$: $k = 0, 1, ..., K$) with uniform mesh spacing Δ_k was employed, such that each grid level, $\mathcal{G}_k$, had $n_k = 2^{k+c+1} + 1$ nodes per unit length in each co-ordinate direction; c is a constant defining the resolution of the coarsest grid level, such that mesh size $\Delta_k = 2^{-(k+c+1)}$. The computations comprised a Full Multigrid W(2,2) cycle, using a coarse grid parameter $c = 4$ and an underlying coarse global grid with $k = 0$, corresponding to uniform grid spacing $\Delta_0 = 1/32$; while relaxation involved a fixed number of pre- and post- Red-Black Gauss-Seidel Newton iterations. By expressing equations (13)–(17) in the form

$$\mathcal{N}_k \mathbf{u}_k^{n+1} = \mathcal{F}_k(\mathbf{u}_k^n) \tag{19}$$

with $\mathcal{N}_k = (\mathcal{N}_k^{\psi}, \mathcal{N}_k^{p}, \mathcal{N}_k^{s}, \mathcal{N}_k^{h}), \mathcal{N}_k^{e})$, $\mathbf{u_k} = (\psi_k, p_k, s_k, h_k, e_k)^T$, and $\mathcal{F}_k = (f_k^{\psi}, f_k^{p}, f_k^{s}, f_k^{h}, f_k^{e})$, on grid level k (n denoting the current time-step and (f_k) corresponding to the right-hand-side of the above equations) the solution to the linearised Newton iterative step can be written in Jacobian form

$$\mathcal{J}_k \Delta \mathbf{u_k} = \mathcal{F}_k - \mathcal{N}_k \ , \tag{20}$$

and solved simultaneously for the increment $\Delta \mathbf{u}_k$ at point (i, j). This is then used to obtain the new approximation for the discretised solution on $\mathcal{G}_k$

$$\tilde{\mathbf{u}}_k^{n+1} = \mathbf{u}_k^{n+1} + \Delta \mathbf{u}_k \ . \tag{21}$$

3.3. Spatial and temporal adaptivity

A key component of the solution strategy is the use of error controlled adaptivity in both space and time; the former automatically determines where fine grids are required to capture the necessary detail in regions involving steep gradients in the solution variables, the latter enables the use of optimum time-stepping increments.

Automatic adaptive grid refinement and de-refinement is achieved with reference to the relative local truncation error $\tau_k^{k-1} \geq \epsilon$, where ϵ is a user-specified tolerance. Large (small) τ_k^{k-1} values indicate regions of significant (insignificant) error between successive grid levels where corresponding further local mesh refinement (de-refinement) is deployed to provide the necessary resolution.

Automatic adaptive time-stepping was imlemented by employing a temporal error control algorithm using predictor-corrector stages, as reported in [17]. The approach proved to be an efficient alternative to existing schemes [18] since it uses second-order accurate time-stepping based on local error estimates obtained from the difference between the current solution and a predicted one, to increase or decrease the time step in a controlled manner whilst concurrently minimising the computational expense associated with repeated time step failure.

4. Results and Discussion

The response of a flexible membrane containing a localised trench topography and the corresponding free-surface disturbance associated with the flow of a gravity-driven thin liquid film is explored and comparisons made with known results for the case of such flow over rigid substrates [10, 9]. Computations were begun from an initial state of a flat flexible membrane supporting a uniformly thin film and allowed to evolve to a steady-state.

The liquid parameters used in all cases are those of water (viscosity, $\mu = 0.001$ Pa s, density, $\rho_f = 1000$ kg m^{-3} and surface tension, $\sigma = 0.07$ N m^{-1}) for a membrane inclined at 30^o to the horizontal with $l_s = w_s = 100$. For an asymptotic film thickness $H_0 = 100\,\mu$m and constant inlet flow rate, $Q_0 = 1.635 \times 10^{-6}$ m^{2}s^{-1}, the above parameters yield a value for the capillary length scale of $L_c = L_0 = 0.78$ mm. $N = 0.12$, while Bo $= 0.085$, shows that the flow and hence free-surface is surface tension dominated. The flexible membrane is assumed to have the following properties: thickness $\lambda = 10\,\mu$m (10% of the asymptotic film height); density, $\rho_m = 1000$ kg m^{-3} under the assumption that the membrane is tissue-like [19]. The topography is defined so as to have a steepness factor, $\gamma = 0.05$, depth, $d_o = -0.25$, width and length $l_t = w_t = 1.54$, and to be centred on $(x_t, y_t) = (30.77, 50)$, consistent with the experiments results reported in [9] and corresponding numerical simulations of [10].

Figure 2 is a comparison of the final steady-state mesh structure and resultant free surface disturbance for both a completely rigid ($\Upsilon = \infty$) and a flexible membrane ($\Upsilon = 1$). Note how, in both cases, a fine mesh is clustered around the topography and follows the free-surface disturbance; throughout the computation to steady-state, dynamic mesh refinement and de-refinement has taken place ensuring accuracy while minimising computational cost and resource. Figure 2(b), shows the characteristic free-surface disturbance which

results when $\Upsilon = \infty$: a *horse-shoe* shaped bow-wave is generated upstream of the topography, together with a free surface depression as the film passes over the topography followed by a peak – or as it is sometimes referred to *downstream surge*. As the trench is finite in length and width, fluid enters it in both stream-wise and span-wise directions due to the lateral pressure gradients resulting from the span-wise curvature of the free-surface. Since in a steady flow, the fluid entering the trench must leave it, the downstream surge simply arises to allow fluid to exit the trench across the shorter width than that across which it entered. Comparing this with the case when the surface is a flexible membrane ($\Upsilon = 1$), shown in Figure 2(d), the overall features are broadly the same but less prominent. In the case of a flexible membrane, the resultant depression over the trench is shallower with a subsequent reduction in the strength of the downstream surge, the consequence being that the downstream disturbance generated is smaller and there is a quicker return to uniform flow conditions downsteam. The difference in the free-surface disturbance arising in each case is shown more clearly as iso-contour plots of ψ in Figure 3.

Figure 4(a) is a plot of the resultant central ($y = 50$) stream-wise free-surface profile for flow over the trench topography when $\Upsilon = 1, 3, 10, 100, \infty$, showing the influence the tension in the membrane has on the shape as given by

$$h^* = (\psi - 1)/|d_0| \ . \tag{22}$$

It reveals significant differences in the vicinity of the topography; a narrower bow-wave is produced the lower the values of Υ, accompanied by a reduction in the depression over the trench and a lowering of the downstream capillary ridge, in line with the observations made above. This is further confirmed by the membrane shape profiles plotted in Figure 4(b), a smaller value of Υ leading to larger membrane deflections, as shown in Figure 4(c), which plots the relative deflection, given by

$$e^* = e/|d_0| \ . \tag{23}$$

The corresponding dominant capillary pressure profiles are shown in Figure 4(d). The large depression in the free-surface across the trench equates to a substantial drop in pressure there resulting in a large positive deflection of the membrane, while the capillary ridge gives rise to an increase in capillary pressure producing a negative membrane deflection. This is summarised in Figure 5.

A similar analysis was performed for the flow over an equal but opposite topographical peak, resulting in analogous observations relating to the effect on free-surface height, membrane shape and membrane deflection. Figures 6 shows colour maps of the resultant steady-state free-surface disturbance when $\Upsilon = \infty$ and $\Upsilon = 1$, together with magnified iso-contour plots of the same in the vicinity of the peak topography.

Having explored the model from the standpoint of single topographical features and shown that the results obtained when $\Upsilon = \infty$ correspond to benchmark solutions obtained for their rigid substrate counterpart, the case of thin film flow over a flexible membrane containing a complex interconnected topography, reminiscent of a micro-circuit, is investigated. The interconnected topography created, with $\gamma = 0.01$, from the addition and subtraction of primitives covers an area given by $l_t(= 0.5) \times w_t(= 0.8)$; $d_0 = 0.05$ defined on a $l_s = w_s = 2$ square solution domain with $L_c = 0.78$ mm and $\beta = 39.1$. Figure 7(a – b) shows the resultant steady-state free-surface colour map and associated rigid membrane, $\Upsilon = \infty$, revealing the disturbance caused by the topography. When these are compared with the corresponding plots for a flexible membrane, $\Upsilon = 1$ shown in Figures 7(c – d), it can be seen that there is a significant reduction in the overall free-surface disturbance in this case, having a positive effect in relation to free-surface planarisation. The peak disturbance is reduced by as much as 53.5% compared to the case when the membrane is rigid. This is a result of significant practical interest since minimising free-surface disturbances is of considerable important to manufacturers with regard to final coat quality. Note the deformation which occurs to the membrane itself when $\Upsilon = 1$, indicated by the iso-contours in Figure 7(d).

5. Conclusions

A model is presented for the flow of gravity-driven thin liquid films over flexible membranes containing surface topography. The accompanying numerical solution strategy, with the capacity to predict both the resulting free-surface disturbance and membrane deflection, represents a useful computational tool for the design of patterned surfaces which fulfill technologic requirements while achieving optimum planarisation. The latter makes the combined effectiveness of model and solver extremely attractive as the need to consider surface flows involving ever smaller topographical features becomes increasingly important.

While previous research considering the simpler two-dimensional problem of thin film flow over span-wise topography has shown that Marangoni stress [20] and electric fields [21] can be used to promote planarisation, the more general three-dimesional case considered here reveals that substrate flexibility can be similarly exploited. Indeed, in the context of mimicking naturally occurring biological surfaces for engineering applications, substrate compliance may turn out to be an added unexpected benefit in determining and hence controlling the flow of thin films on delicate tribological textured surfaces.

References

[1] **Vincent, J.V.F.** Stealing ideas from nature, In *Deployable structures* (Springer, Ed. S. Pellegrino), 2001, 51-58.

[2] **Abbott, S.J.,** and **Gaskell, P.H.** Mass production of bio-inspired structured surfaces, *Proc. I.Mech.E Part C*, **221**, 2007, 1181-1191.

[3] **Quere, D.** Wetting and roughness, *Annu. Rev. Mater. Res.*, **38**, 2008, 71-99.

[4] **Ho, W.K., Tay, A., Lee, L.L.,** and **Schaper, C.D.** On control of resist film uniformity in the microlithographic process, *Contro; Eng. Prac.*, 2004, **12**(7) 881-892).

[5] **Clarke, A.** Coating on a rough surface, *A.I.Ch.E. Journal*, 2002, **48**, 2149-2156.

[6] **Walters, D.R.** Disguising the leaf surface: the use of leaf coatings for plan disease control, *Euro. J. Plant Pathology*, 2006, **114**, 255-260.

[7] **Garver, D.P.,** and **Grotberg, J.B.** The dynamics of localised surfactant on a thin-film, *J. Fluid Mech.*, 1990, **213**, 127-148.

[8] **Mueller, T.** Biomimetics, *National Geographic*, 2008, April, 68-91.

[9] **Decre, M.J.,** and **Baret, J.C.** Gravity-driven flows of viscous liquids over two-dimensional topographies. *J. Fluid Mech.*, 2003, **487**, 147-166.

[10] **Gaskell, P.H., Jimack, P.K., Sellier, M., Thompson, H.M.,** and **Wilson, M.C.T.** Gravity-driven flow of continuous thin lliquid films on non-porous subsrates with topography. *J. Fluid Mech.*, 2004, **509**, 253-280.

[11] **Blyth, M.G.,** and **Pozrikidis, C.** Film flow down an inclined plane over a three-dimensional obstacle, *Phys. Fluids*, 2006, **18**, Article No. 052104.

[12] **Lee, Y.C., Thompson, H.M,** and **Gaskell, P.H.** An efficient adaptive multigrid algorithm for predicting thin film flow on surfaces containing localised topographic features. *Comp. Fluids*, 2007, **36**, 838-855.

[13] **Singh, R.A., Yoon, E-S., Kim, H.J., Kim, J., Jeong, H.E.,** and **Suh, K.Y.** Replication of surfaces of natural leaves for enhanced microscale tribological property, *Mat. Sci. Eng. C*, 2007, **27**, 875–879.

[14] **Linn, N.C., Sun, C-H., Jiang, P.,** and **Jiang, B.** Self-assembled biomimetic antireflection coatings, *App. Phys. Letts.*, 2007, **91**, Article No. 101108.

[15] **Ko, H.C., Stoykovich, M.P., Song, J., Matyarchuk, V., Choi, W.M., Yu, C-J., Geddes III, J.B., Xiao, J., Huang, Y.,** and **Rogers, J.A.** A hemispherical electronic eye camera based on compressible silicon optoelectronics, *Nature*, 2008, **454**(7), 748-753.

[16] **Bertozzi, A.,** and **Brenner, M.P.** Linear stability analysis and transient growth in driven contact lines, *Phys. Fluids*, 1997, **9**, 530-539.

[17] **Gaskell, P.H., Jimack, P.K., Sellier, M.,** and **Thompson, H.M.** Efficient and accurate time adaptive multigrid simulation of droplet spreading. *Int. J. Num. Meth. Fluids.*, 2004, **45**, 1161-1186.

[18] **Diez, J.A.,** and **Kondic, L.** Computing three-dimensional thin film flows including contact lines. *J. Comp. Phys.*, 2002, **183**, 274-306.

[19] **Matar, O.K.,** and **Kumar, S.K.** Rupture of a surfactant-covered thin liquid film on a flexible wall, *SIAM, J. Appl. Math.*, 2004, **64**(6) 2144-2166.

[20] **Gramlich, C.M., Kalliadasis, S.,** and **Homsy, G.M.** Optimal leveling of flow over one-dimensional topography by Marangoni stresses, *Phys. Fluids*, 2002, **14**, 1841-1850.

[21] **Tseluiko, D., Blyth, M.G., Papageorgiou, D.T.,** and **Vanden-Broeck, J-M.** Electrified viscous thin film flow over topography, *J. Fluid Mech.*, 2008, **597**, 449-475.

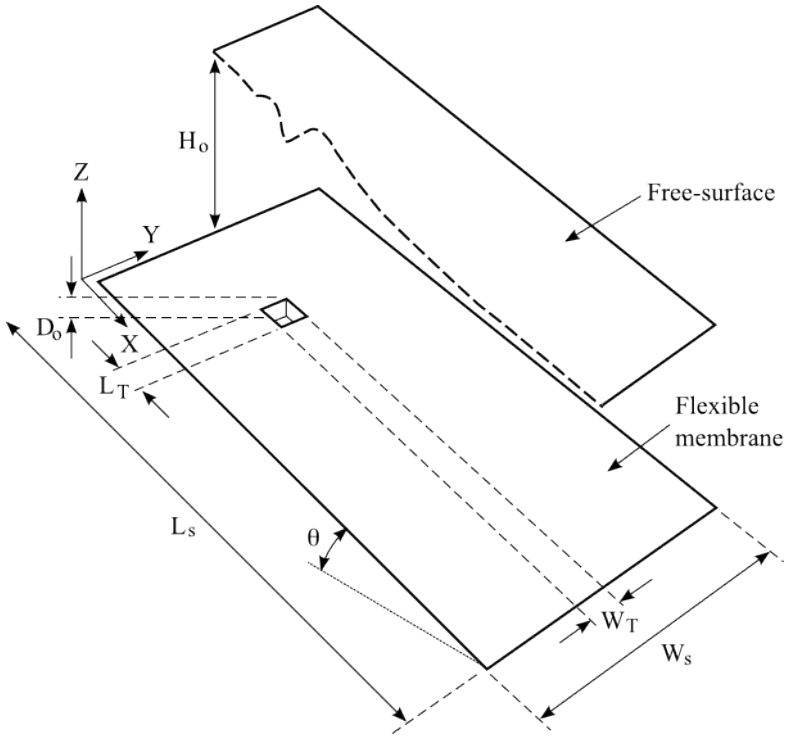

Figure 1: Schematic of the flow of a thin liquid film over a flexible membrane inclined at θ to the horizontal and containing a trench topography (length L_T, width W_T, depth D_0).

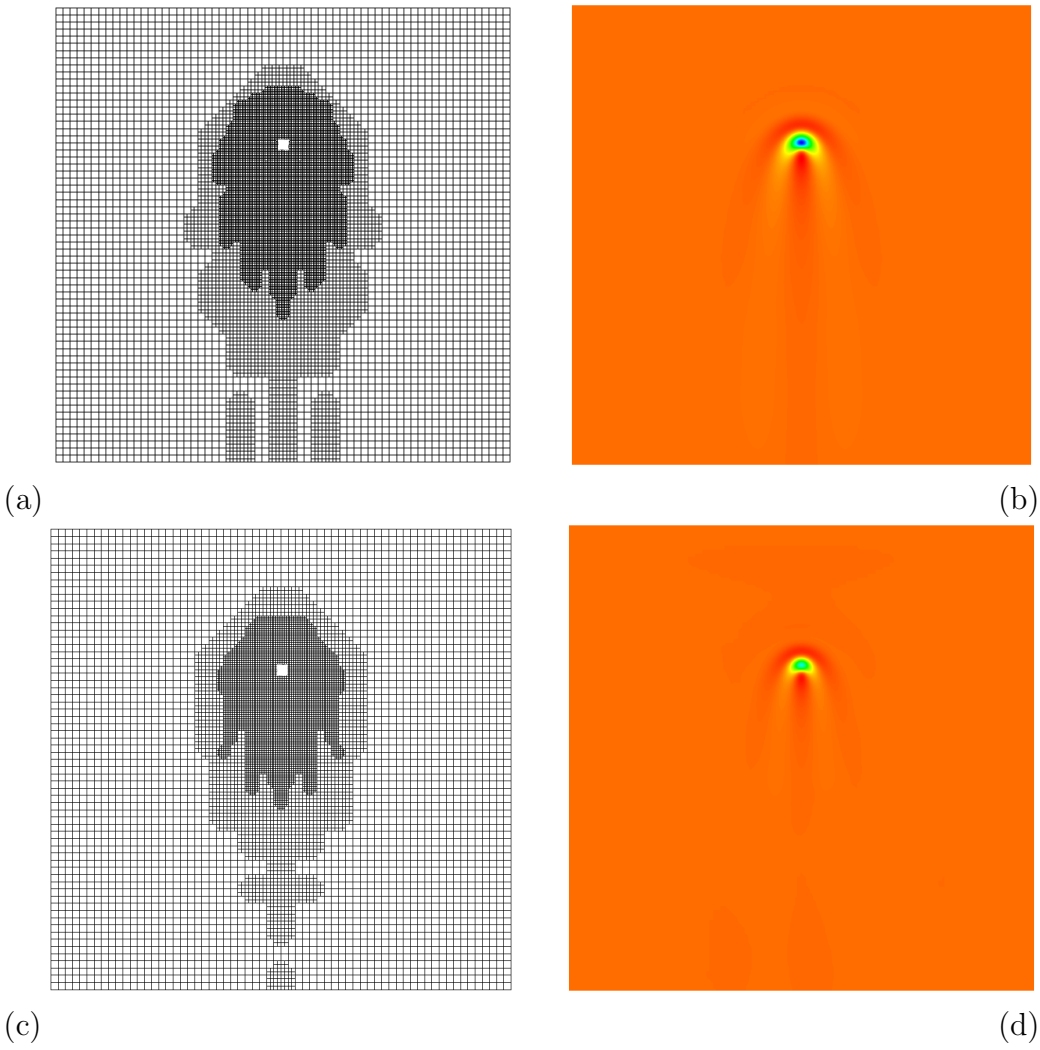

Figure 2: Steady-state flow over a localised square trench topography ($l_t = w_t = 1.54$ and $d_0 = -0.25$ centred at $(x_t, y_t) = (30.77, 50)$, error tolerance $\epsilon = 0.1\tau$) for: $\Upsilon = \infty$ [final adaptive mesh structure (a), free-surface colour map of ψ (b)]; $\Upsilon = 1$ [final adaptive mesh structure (c), free-surface colour map of ψ (d)]. The direction of flow is from top to bottom.

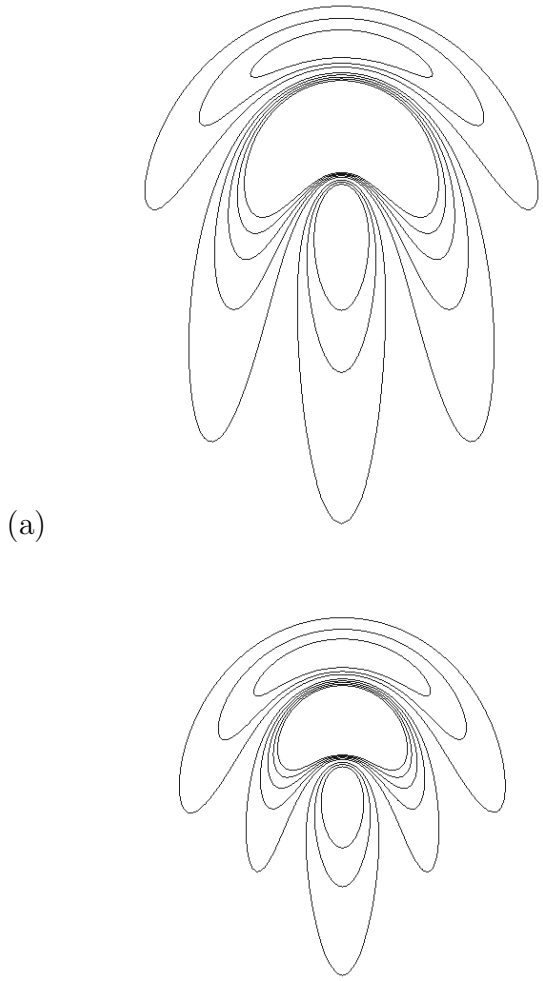

Figure 3: Magnified resultant iso-contour profiles of ψ: (a) $\Upsilon = \infty$; (b) $\Upsilon = 1$. Contour values are chosen so as to be equal in magnitude and the direction of flow is from top to bottom.

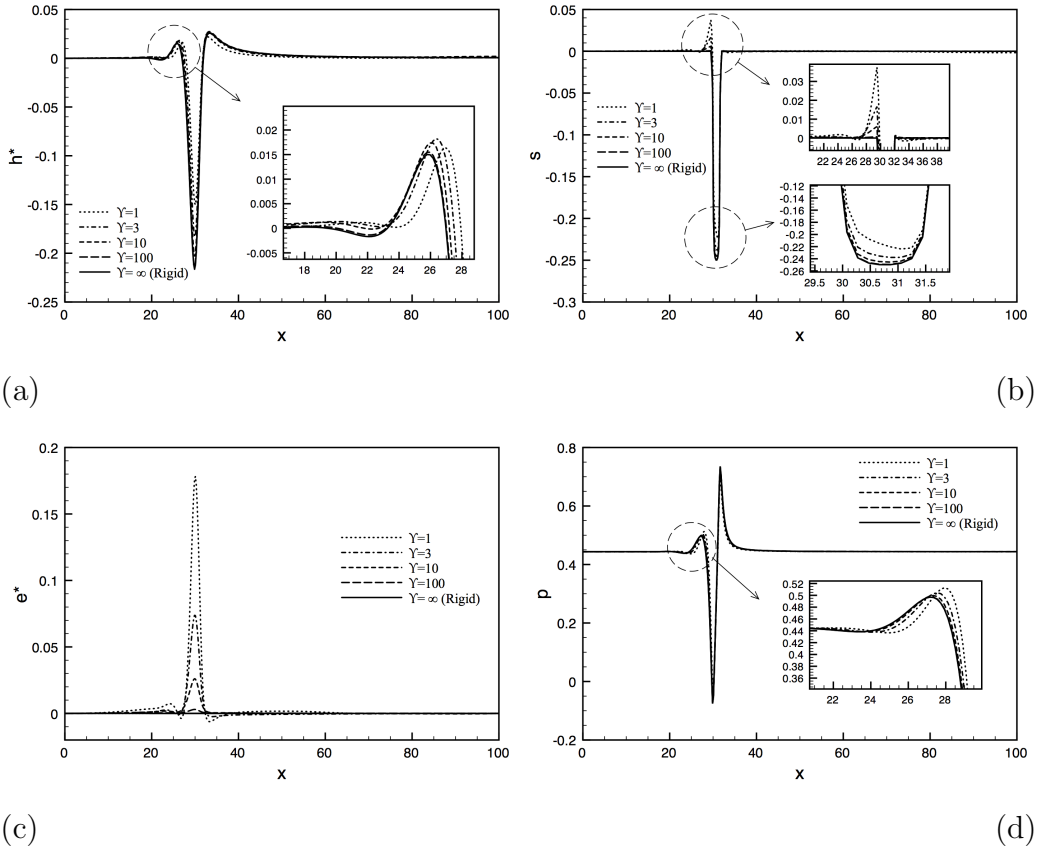

Figure 4: Central stream-wise profiles ($y = 50$) for different values of Υ: (a) free-surface heights, h^*; (b) membrane shape, s; (c) membrane deflection, e^*; (d) capillary pressure, p. The direction of flow is from left to right.

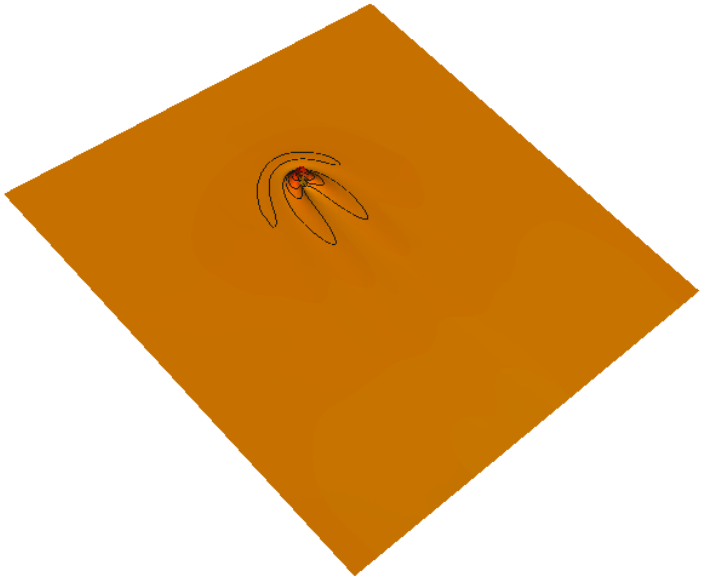

Figure 5: Steady-state membrane profile; colour map plus iso-contours for flow over a trench topography when $\Upsilon = 1$. Contour values are chosen to be equal in magnitude and the direction of flow is from top left to bottom right.

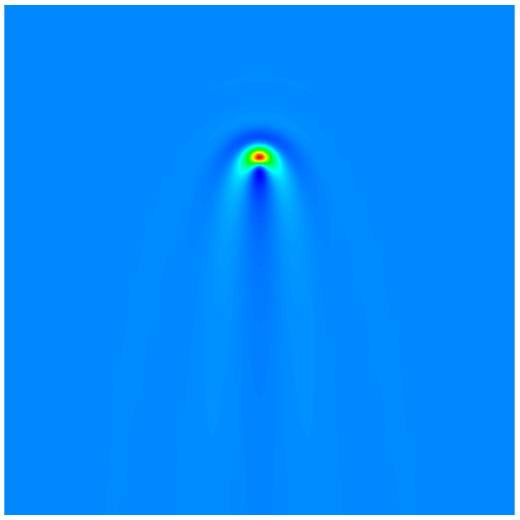

(a)

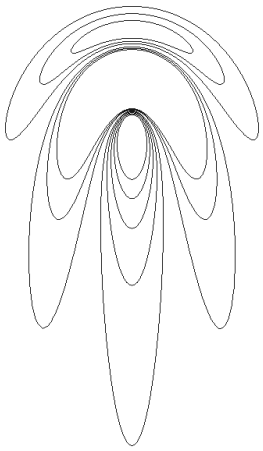

(b)

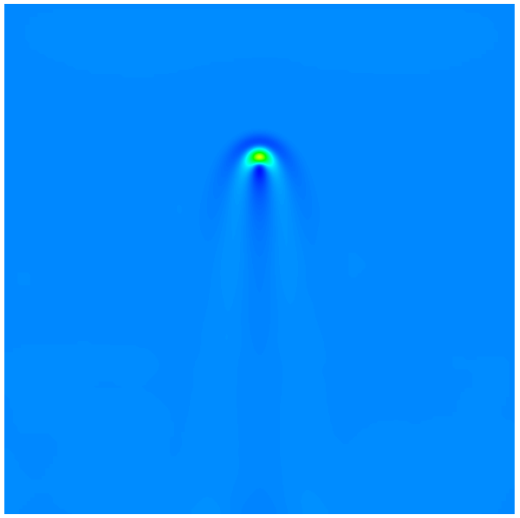

(c)

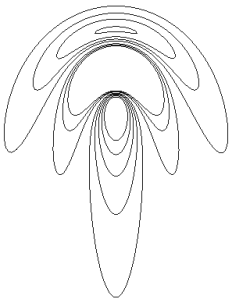

(d)

Figure 6: Steady-state flow over a localised square peak topography ($l_t = w_t = 1.54$ and $d_0 = 0.25$ centred at $(x_t, y_t) = (30.77, 50)$, error tolerance $\epsilon = 0.1\tau$) for: $\Upsilon = \infty$ (a); $\Upsilon = 1$ (c). Corresponding magnified iso-contour profiles of ψ in the vicinity of the topography for: $\Upsilon = \infty$ (b); $\Upsilon = 1$ (d). The direction of flow is from top to bottom.

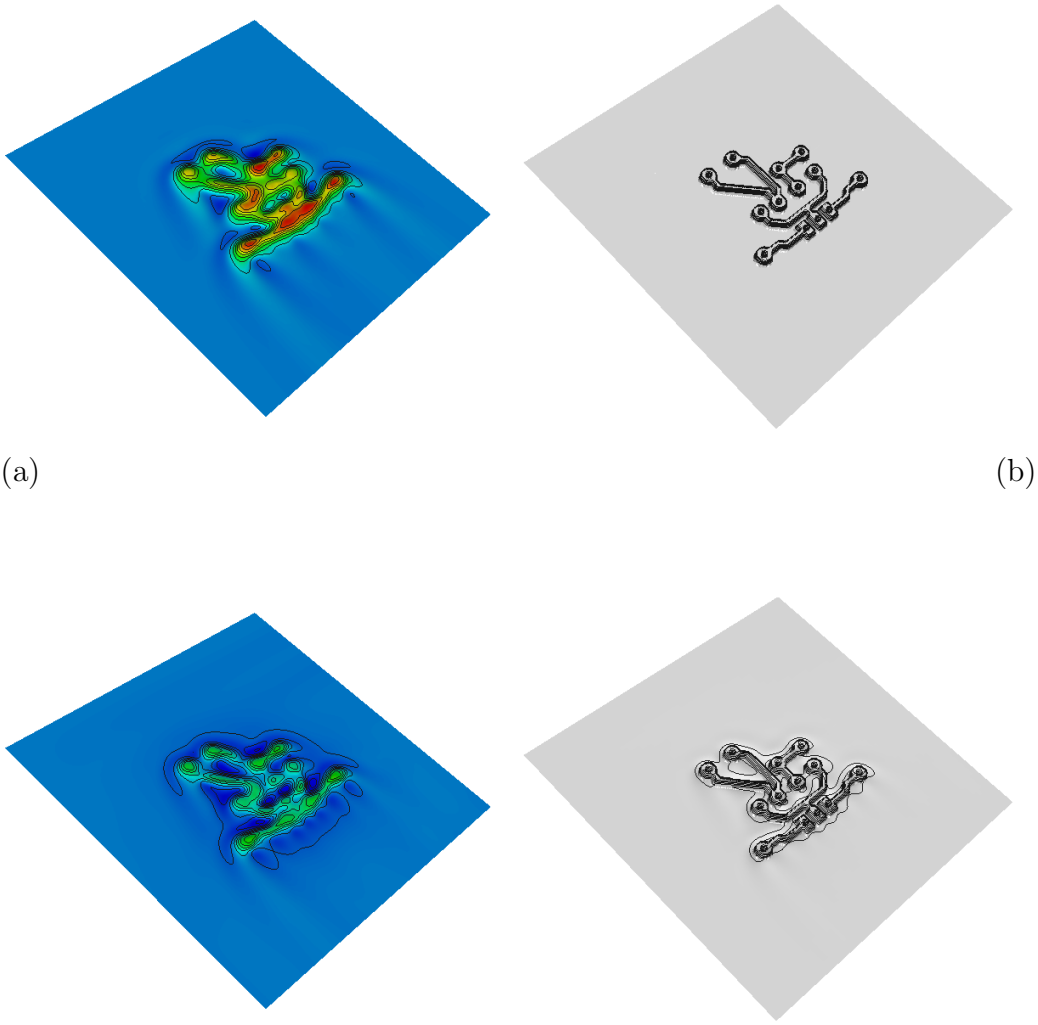

(a) (b)

(c) (d)

Figure 7: Colour maps and iso-contours for flow over complex surface topography (micro-circuitry): $\Upsilon = \infty$ (top); $\Upsilon = 1$ (bottom). Free surface disturbance (a) and (c); membrane profile (b) and (d). Contour values are chosen to be equal in magnitude and the direction of flow is from top left to bottom right in each case.